

Cite this: *J. Mater. Chem. A*, 2018, 6, 16213

# Simultaneous *in situ* reduction and embedment of Cu nanoparticles into TiO<sub>2</sub> for the design of exceptionally active and stable photocatalysts†

Serene Wen Ling Ng,<sup>a</sup> Minmin Gao,<sup>a</sup> Wei Li Ong,<sup>a</sup> Kane Jian Hong Lim,<sup>ab</sup> Connor Kang Nuo Peh<sup>a</sup> and Ghim Wei Ho<sup>id</sup>\*<sup>acd</sup>

Efficient charge separation for a photocatalyst can be realized *via* addition of a co-catalyst, whereby most conventional techniques, *i.e.*, deposition–precipitation, photoreduction, hydrothermal and vapour phase deposition result typically in surface loading effects. Moreover, the loading amount is deliberately kept nominal (below 10 wt%) as excessive loading causes both agglomeration and light blocking issues which limit the performance and stability of the photocatalyst. This work demonstrates one-pot *in situ* synthesis towards interdispersion and inclusion of a high concentration (Cu : TiO<sub>2</sub> weight ratio > 1) of a Cu NP co-catalyst into TiO<sub>2</sub> nanosheets without compromising its critical dispersivity and light absorption properties. The exceptional photocatalytic H<sub>2</sub> performance of 16.1 ± 0.35 mmol g<sup>-1</sup> h<sup>-1</sup> stems from the embedment and confinement of the small Cu NPs within the TiO<sub>2</sub> matrix which facilitates a shorter diffusion distance, thereby increasing the number of electrons available for catalytic reactions. Thus, this work highlights a facile approach towards optimal interfacing of the hybrid catalyst constituents to mitigate the limited interfacial contact and charge transfer challenges commonly faced in photocatalyst design.

Received 2nd May 2018

Accepted 25th July 2018

DOI: 10.1039/c8ta04052d

rsc.li/materials-a

## Introduction

Solar to chemical energy conversion through the use of photocatalysts has been an appealing approach as one sustainable route to reduce our dependency on non-renewable fossil fuels. This has led to increased attention towards using photocatalysts for H<sub>2</sub> production from water splitting in recent research.<sup>1–6</sup> TiO<sub>2</sub>-based photocatalysts have been extensively studied due to their low toxicity, high stability and low cost.<sup>6–11</sup> However, there are two main limitations in the photocatalytic performance of TiO<sub>2</sub> which include its poor electron–hole pair separation due to the fast recombination rate<sup>12,13</sup> and the limited light absorption range in the UV region.<sup>14,15</sup> Extensive studies such as the addition of co-catalysts to improve charge transfer,<sup>16</sup> bandgap engineering through doping<sup>17</sup> and coupling materials to shift the light absorption<sup>18–20</sup> have been carried out to overcome the aforementioned limitations. Thus, synthesizing a photocatalyst

with efficient charge separation properties to reduce the recombination rate and increase the visible light absorption is paramount to achieving superior photocatalytic performance.

To reduce the recombination rate, co-catalysts are usually added to improve the charge separation of the electron–hole pair.<sup>21–25</sup> Since the surfaces of co-catalysts are required to be exposed to participate in the redox reaction,<sup>26</sup> small noble metal nanoparticles (NPs) (<10 nm) such as Pt, Au and Ag are usually deposited atop the photocatalyst as electron sinks to enhance electron–hole pair separation.<sup>27–30</sup> Moreover, small metal NPs have a large surface area, which provides more active sites for the photocatalytic reaction to take place, thereby enhancing the photocatalytic performance.<sup>31</sup> Surface loading of the co-catalyst can be done by a few methods: (i) deposition–precipitation method,<sup>32</sup> (ii) photoreduction method,<sup>33</sup> and (iii) loading of the metal particles through vapour phase deposition.<sup>34</sup> Alternatively, loading of the metal co-catalyst can also be done using hydrothermal treatment, where reducing agents are added to reduce the precursor and deposit metal particles on the photocatalyst.<sup>21,22</sup> Most of these surface loading methods, however, only loosely load or deposit co-catalyst particles on the surface of the photocatalyst, which would likely result in subsequent clustering and leaching issues.<sup>35</sup> Moreover, the loading amount is usually kept nominal (below 10 wt%) as excessive loading causes both agglomeration and light blocking effects which limit the performance of the photocatalyst.<sup>35</sup> Hence, the deposition of small NPs in a large quantity with minimal

<sup>a</sup>Department of Electrical and Computer Engineering, National University of Singapore, 4 Engineering Drive 3, 117583, Singapore. E-mail: elehw@nus.edu.sg

<sup>b</sup>NUS Graduate School for Integrative Sciences and Engineering, Centre for Life Sciences (CeLS), #05-01, 28 Medical Drive, 117456, Singapore

<sup>c</sup>Institute of Materials Research and Engineering, A\*STAR (Agency for Science, Technology and Research), 3 Research Link, 117602, Singapore

<sup>d</sup>Engineering Science Programme, National University of Singapore, 9 Engineering Drive 1, 117575, Singapore

† Electronic supplementary information (ESI) available. See DOI: 10.1039/c8ta04052d

agglomeration and maximal interfacial coupling remains particularly challenging due to the difficulties in controlling the co-catalyst formation during the synthesis.

Herein, this work presents an easy method using one-step hydrothermal to homogeneously interdisperse a Cu NP co-catalyst into TiO<sub>2</sub> sheets in large quantities (Cu : TiO<sub>2</sub> ratio > 1) without compromising its dispersivity for enhanced photocatalytic H<sub>2</sub> production. This co-catalyst deposition approach demonstrates simultaneous *in situ* reduction and embedment of small metal NPs into the photocatalyst using a one-pot synthesis method. Cu NPs are chosen as the co-catalyst of TiO<sub>2</sub> due to their low cost and antimicrobial properties compared to other noble metals.<sup>36–38</sup> The Cu/TiO<sub>2</sub> hybrid is designed to accommodate copious Cu NPs, serving as electron sinks to aid charge separation. In addition, the *in situ* deposition strategy of Cu in TiO<sub>2</sub> sheets warrants the immobilization of the co-catalysts, leading to minimal clustering and leaching, and hence provides excellent stability for prolonged usage. The homogeneous interdispersion of the co-catalyst within the photocatalyst also ensures close interfacial contact between the TiO<sub>2</sub> and Cu NPs, which enhances the charge migration to reduce recombination. This work showcases a facile pathway towards the design and tailoring of co-catalysts that are homogeneously embedded in the photocatalyst for enhanced surface and interface dominated photoredox reactivity.

## Experimental sections

### Synthesis of CuO

In solution A, 0.2 g of copper acetate (Acros Organics) was added to 10 ml of deionized (DI) water and stirred at 500 rpm until complete dissolution. Next, 1.2 g of polyvinylpyrrolidone (PVP, Fisher Scientific) of  $M_w \sim 10\,000$  was added to solution A and left to stir until complete dissolution. In solution B, 0.2 g of ascorbic acid (Sigma Aldrich) was dissolved in 10 ml of DI water. This was added to solution A and stirred at 500 rpm for 1 min. Then, the mixture was centrifuged three times at 2500 rpm for 3 min. The resulting product was eventually dried at 60 °C and left in a furnace at 400 °C for 4 hours with a ramp rate of 2 °C min<sup>-1</sup>. The powder was collected for further use.

### Synthesis of TiO<sub>2</sub> and Cu/TiO<sub>2</sub>

Pure TiO<sub>2</sub> samples were synthesized by adding 20 ml of pure ethanol, followed by 160 µl of titanium tetraisopropoxide (TTIP, Sigma Aldrich) and 200 µl of diethylenetriamine (DETA, Alfa Aesar). For Cu/TiO<sub>2</sub> samples, 15 mg of CuO was added to 20 ml of pure ethanol, followed by 60 µl of TTIP and varying amounts of DETA. The mixtures were left to sonicate and stir for 5 min. The amounts of DETA were varied at 70, 90, 110 and 130 µl and the samples were labelled Cu/TiO<sub>2</sub>-1, Cu/TiO<sub>2</sub>-1.3, Cu/TiO<sub>2</sub>-1.6 and Cu/TiO<sub>2</sub>-1.9, respectively. The solutions were then transferred to a Teflon-lined autoclave with a capacity of 50 ml and heated at 200 °C for 17 hours. The product was washed three times with ethanol, and then eventually dried at 60 °C and annealed at 450 °C for 2 hours in a N<sub>2</sub> gas environment with a ramp rate of 2 °C min<sup>-1</sup>.

### Synthesis of Cu/TiO<sub>2</sub> (surface-load)

Cu NPs were synthesized by an aqueous precipitation method.<sup>39</sup> The Cu/TiO<sub>2</sub> (surface-load) nanocomposite was prepared by adding a desired amount of Cu NPs to TiO<sub>2</sub> powder in 20 ml ethanol to achieve various Cu loading %. The solution was stirred in a water bath at 90 °C for 3 h. Next, the samples were annealed at 450 °C for 2 hours in a N<sub>2</sub> gas environment with a ramp rate of 2 °C min<sup>-1</sup>. The samples were irradiated under a UV light source (365 nm) with a light intensity of 44 mW cm<sup>-2</sup> for 1 hour before using them for any measurements.

### Materials characterization

Scanning electron microscopy (SEM) characterization was carried out using a JEOL FEG JSM 7001F field-emission SEM operating at 15 kV. The crystalline structures were analyzed using transmission electron microscopy (TEM, Phillips FEG CM300) performed at 200 kV and X-ray diffraction (XRD, D5005 Bruker X-ray diffractometer equipped with graphite-monochromated Cu K $\alpha$  radiation at  $\lambda = 1.541 \text{ \AA}$ ). The Cu concentration was determined using inductively coupled plasma optical emission spectrometry (iCAP 7400 ICP-OES analyzer, Thermo Fisher Scientific). Photoluminescence (PL) measurements were carried out using a Shimadzu RF-5301 PC spectrofluorophotometer. The type of volatile organic compound (VOC) present in the reactor was determined by extracting 100 µl of the reaction mixture with a gas-tight syringe and injecting into a gas chromatographer mass spectrometer (Shimadzu GCMS-QP2010 Ultra).

### Photocatalytic H<sub>2</sub> measurements

The H<sub>2</sub> evolution measurements were carried out using 1 mg of photocatalyst and 10 ml DI water (containing 10 wt% glycerol) in a quartz vial. The quartz vial was illuminated with a UV light source (365 nm) with a light intensity of 44 mW cm<sup>-2</sup> and a Xe lamp (Excelitas, PE300BFM) with a light intensity of 100 mW cm<sup>-2</sup> equipped with a 400 nm long-pass filter. The reaction mixture was purged with Ar gas for 10 min prior to measurements. The reaction mixture was drawn (100 µl) using a syringe to sample the gas composition using a gas chromatograph (Shimadzu, GC-2014AT).

### Photoelectrochemical and concurrent H<sub>2</sub> measurements

Photoelectrochemical (PEC) samples were prepared on fluorine doped tin oxide (FTO) substrates (QZ hybrid supplies, <10  $\Omega \text{ sq}^{-1}$ ) using the drop casting method. Mixtures were prepared from the various nanostructured samples and ethanol, which were then drop cast on the surface of FTO glass. The coated FTO glass substrates were dried at 60 °C on a hot plate. The PEC measurements were carried out with an electrochemical workstation (CHI-660E) with 2 electrode configuration, using the prepared photoanode on FTO glass and Pt as a counter electrode with zero bias in 10 wt% glycerol aqueous solution. The light source used was a UV LED (365 nm) with a light intensity of 44 mW cm<sup>-2</sup>. The reaction mixture was purged with Ar gas for 10 min prior to measurements. The

reaction mixture was drawn (100  $\mu\text{l}$ ) using a syringe to sample the gas composition using a gas chromatograph (Shimadzu, GC-2014AT).

### Electrochemical impedance spectroscopy (EIS)

The samples were prepared on FTO substrates (QZ hybrid supplies,  $<10 \Omega \text{ sq}^{-1}$ ) using the drop casting method. Mixtures were prepared from the various nanostructured powders and ethanol (5% Nafion), which were then drop cast on the surface of FTO glass. The coated FTO glass substrates were dried at 60  $^{\circ}\text{C}$  on a hot plate. EIS tests were performed with a frequency loop from 100 kHz to 0.1 Hz by applying a sine wave with an amplitude of 5 mV at open circuit potential, using the prepared photoanode on FTO glass and Pt as a counter electrode in 0.25 M  $\text{Na}_2\text{SO}_4$  and 5% glycerol solution. The EIS spectra were measured both in the dark and under UV LED irradiation (365 nm) with a light intensity of 44  $\text{mW cm}^{-2}$ .

## Results and discussion

Uniform CuO spheres were synthesized with an average size of  $\sim 600 \text{ nm}$  (Fig. S1 $\dagger$ ). CuO was used as the Cu source for the synthesis of Cu/TiO<sub>2</sub> (Cu being embedded in TiO<sub>2</sub> sheets) as illustrated in Fig. 1. During the hydrothermal treatment, TTIP acts as the Ti precursor and DETA aids in the formation of TiO<sub>2</sub> sheets while ethanol was used as the reducing agent to reduce CuO to Cu. The reduction process was confirmed using GC-MS which indicated the presence of acetaldehyde (oxidation of ethanol) after the synthesis. The reduction process was also validated by XRD (Fig. S2 $\dagger$ ) before and after the hydrothermal treatment. Concurrently, the dissolution and reprecipitation of CuO into small Cu NPs occur, which then become embedded and distributed evenly in the TiO<sub>2</sub> sheets during the synthesis process. These small embedded Cu NPs are ideal for superior photocatalytic H<sub>2</sub> production due to; (i) an increase in the surface area due to the small particle size, leading to more active sites for photocatalytic reactions;<sup>31</sup> (ii) the immobilization of Cu NPs inhibits clustering and leaching, providing excellent stability for prolonged usage; (iii) the embedment of Cu NPs which ensures close interfacial contact of TiO<sub>2</sub> and Cu NPs, thus

enhancing charge migration from the TiO<sub>2</sub>/Cu interface to the Cu surface for catalytic reactions.

Next, different amounts of DETA were introduced during the hydrothermal process with amounts of 70, 90, 110 and 130  $\mu\text{l}$ . The samples were labelled Cu/TiO<sub>2</sub>-1, Cu/TiO<sub>2</sub>-1.3, Cu/TiO<sub>2</sub>-1.6 and Cu/TiO<sub>2</sub>-1.9, respectively, and Cu concentrations were determined by ICP-OES. The weight ratio of TiO<sub>2</sub> : Cu was found to be approximately 1 : 1, 1 : 1.3, 1 : 1.6 and 1 : 1.9, respectively. The samples were characterized by SEM (Fig. S3 $\dagger$ ) and no distinct differences in the Cu NP size can be seen. As such, TEM was used to image the samples to analyze the Cu NP dimensions (Fig. S4 to S8 $\dagger$ ). A graph detailing the Cu NP size distributions of Cu/TiO<sub>2</sub>-1.3, Cu/TiO<sub>2</sub>-1.6 and Cu/TiO<sub>2</sub>-1.9 was plotted (Fig. 2a). The graph reveals the peak particle sizes as approximately  $\sim 3 \text{ nm}$ ,  $\sim 4 \text{ nm}$  and  $\sim 2 \text{ nm}$ , respectively. All samples were characterized with XRD (Fig. S9 $\dagger$  and 2b) and found to exhibit both the anatase phase of TiO<sub>2</sub> and highly crystalline Cu NPs.

Cu/TiO<sub>2</sub> (surface-load) of the same Cu concentration was synthesized using the deposition approach for comparison with Cu/TiO<sub>2</sub>-1.6. In Fig. 2c, Cu NPs are not evident in the SEM image for Cu/TiO<sub>2</sub>-1.6 while Fig. 2d clearly indicates Cu NP clusters on the surface of the TiO<sub>2</sub> sheets for Cu/TiO<sub>2</sub> (surface-load). This suggests that the Cu NPs are highly likely to be interdispersed and embedded within the TiO<sub>2</sub> sheets for the Cu/TiO<sub>2</sub>-1.6 sample. To verify the hypothesis further, TEM was performed and NPs were seen in both Cu/TiO<sub>2</sub>-1.6 and Cu/TiO<sub>2</sub> (surface-load) (Fig. 2e and f, respectively), as revealed by the dark spots on the sheets in the TEM images. In addition, it is noteworthy that the lattice fringes of Cu are found within the fringes of TiO<sub>2</sub> with no boundaries surrounding the Cu (Fig. 2g) unlike Cu/TiO<sub>2</sub> (surface-load) (Fig. 2h). It was noted that the XRD plot of Cu/TiO<sub>2</sub> (surface-load) exhibited Cu peaks (Fig. S10 $\dagger$ ) while the lattice fringes shown in Fig. 2h correspond to the (111) plane of Cu<sub>2</sub>O instead of Cu. This suggests the occurrence of surface oxidation which is common for Cu materials.<sup>35</sup>

The H<sub>2</sub> production rates of the samples synthesized with different DETA amounts were compared. It was noted that the H<sub>2</sub> production rates increase with increasing Cu NP sizes where Cu/TiO<sub>2</sub>-1, Cu/TiO<sub>2</sub>-1.3 Cu/TiO<sub>2</sub>-1.6, and Cu/TiO<sub>2</sub>-1.9 exhibited H<sub>2</sub> production rates of 5.9, 8.6, 16.7 and 6.3  $\text{mmol g}^{-1} \text{ h}^{-1}$ , respectively (Fig. 3a). The optimal Cu NP size for enhanced

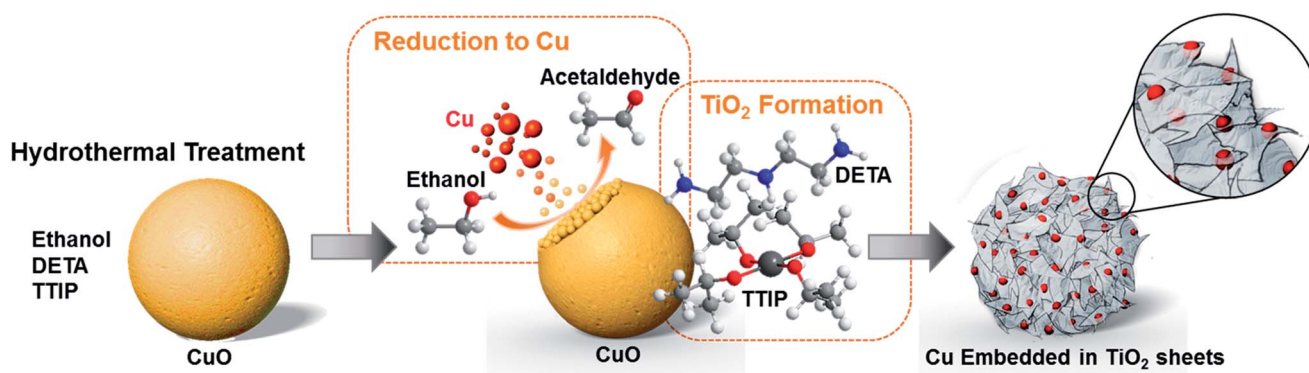


Fig. 1 Schematic diagram of the synthesis of Cu embedded TiO<sub>2</sub> sheets.

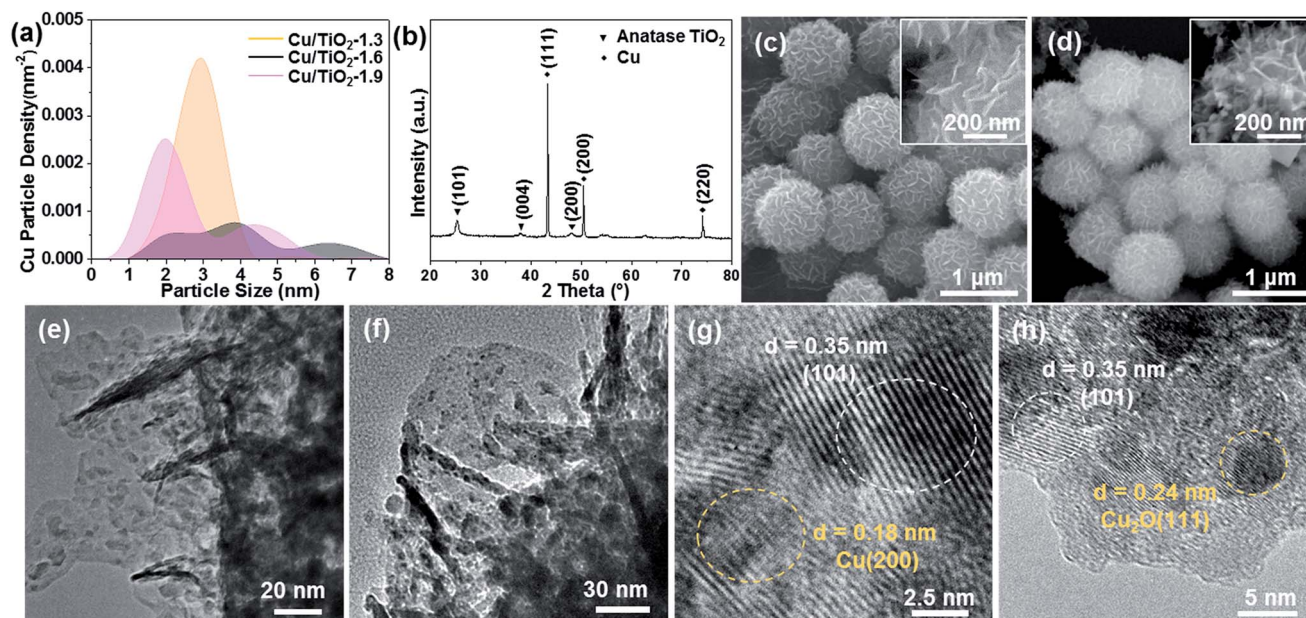


Fig. 2 (a) Graph of Cu particle density against particle size for Cu/TiO<sub>2</sub>-1.3, Cu/TiO<sub>2</sub>-1.6 and Cu/TiO<sub>2</sub>-1.9. (b) XRD of Cu/TiO<sub>2</sub>-1.6. (c and d) SEM image and high magnification SEM image (inset) of Cu/TiO<sub>2</sub>-1.6 and Cu/TiO<sub>2</sub> (surface-load), respectively. (e and f) TEM images of Cu/TiO<sub>2</sub>-1.6 and Cu/TiO<sub>2</sub> (surface load), respectively. (g and h) HRTEM images of Cu/TiO<sub>2</sub>-1.6 and Cu/TiO<sub>2</sub> (surface-load), respectively.

photocatalytic H<sub>2</sub> production was found to be a broad distribution with the peak size at 4 nm while the Cu : TiO<sub>2</sub> concentration was found to be ~1.6. The stability of Cu/TiO<sub>2</sub>-1.6 has

also been demonstrated as shown in Fig. 3b. It was noted that the H<sub>2</sub> performances were consistent over 4 cycles, with a H<sub>2</sub> generation rate of  $16.1 \pm 0.35 \text{ mmol g}^{-1} \text{ h}^{-1}$  (Fig. 3b), exhibiting a stable photocatalytic activity for Cu/TiO<sub>2</sub>-1.6. The apparent quantum yield (AQY) was calculated to be 9.82% for Cu/TiO<sub>2</sub>-1.6 which is comparable to previously reported values<sup>40,41</sup> (please refer to the ESI† for the details of the calculation of AQY). Next, the H<sub>2</sub> generation rates of TiO<sub>2</sub> and Cu/TiO<sub>2</sub> (surface-load) (with a Cu : TiO<sub>2</sub> concentration of ~1.6) were also investigated. TiO<sub>2</sub> and Cu/TiO<sub>2</sub> (surface-load) exhibited H<sub>2</sub> generation rates of 0.95 and 5.9 mmol g<sup>-1</sup> h<sup>-1</sup>, respectively (Fig. 3a), where Cu/TiO<sub>2</sub> (surface-load) displayed a H<sub>2</sub> generation rate which is 6.2 times higher than that of TiO<sub>2</sub>. Comparing both samples to Cu/TiO<sub>2</sub>-1.6, Cu/TiO<sub>2</sub>-1.6 has a H<sub>2</sub> generation rate that is 16.9 times and 2.7 times higher than that of TiO<sub>2</sub> and Cu/TiO<sub>2</sub> (surface-load), respectively. The increase in H<sub>2</sub> production rates after the addition of Cu NPs is ascribed to the presence of electron sinks for enhanced electron-hole pair separation.<sup>2,22</sup> This suppresses the fast recombination rate of TiO<sub>2</sub>, allowing more electrons to be available for H<sub>2</sub> catalytic reactions, thus enhancing the H<sub>2</sub> production rate. The superior H<sub>2</sub> production activity of Cu/TiO<sub>2</sub>-1.6 is attributed to the evenly distributed and embedded Cu NPs compared to the clustered Cu NPs on Cu/TiO<sub>2</sub> (surface-load). For the Cu/TiO<sub>2</sub>-1.6 sample, the Cu NPs are trapped within the TiO<sub>2</sub> sheets, and this allows for faster migration of electrons from the TiO<sub>2</sub>/Cu interface to the Cu surface, leading to an enhanced H<sub>2</sub> production rate.

As Cu is prone to oxidation, Cu/TiO<sub>2</sub>-1.6 was further tested for its stability after leaving it under ambient conditions for 2 months. The TEM images (Fig. S11†) show surface oxidation as CuO lattice fringes were seen instead of Cu. XPS was also carried out and shake-up peaks can be observed (Fig. S12†) which

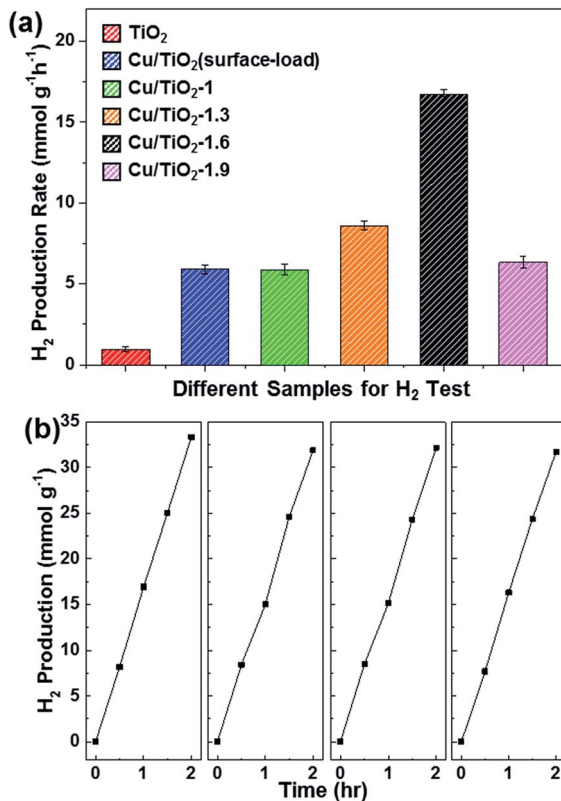


Fig. 3 (a) H<sub>2</sub> production rates of TiO<sub>2</sub>, Cu/TiO<sub>2</sub> (surface-load), Cu/TiO<sub>2</sub>-1, Cu/TiO<sub>2</sub>-1.3, Cu/TiO<sub>2</sub>-1.6 and Cu/TiO<sub>2</sub>-1.9 under UV + visible light for 2 hours. (b) H<sub>2</sub> production cycling test for Cu/TiO<sub>2</sub>-1.6.

indicates the presence of CuO while the XRD plot in Fig. S13† exhibited strong Cu peaks. Since XPS is a surface technique while XRD is a bulk characterization technique, it is believed that the CuO is present only at the surface of the Cu nanoparticles. Nevertheless, Cu/TiO<sub>2</sub>-1.6 H<sub>2</sub> production activity was investigated for 3 additional cycles (Fig. S14a†). The H<sub>2</sub> production is still consistent with a H<sub>2</sub> generation rate of  $16.3 \pm 0.19 \text{ mmol g}^{-1} \text{ h}^{-1}$ , indicating that Cu/TiO<sub>2</sub>-1.6 is stable and suitable for prolonged usage despite the surface oxidation of Cu. On the other hand, H<sub>2</sub> production measurements for Cu/TiO<sub>2</sub> (surface-load) were also repeated for 3 cycles (Fig. S14b†) and the H<sub>2</sub> production rate dropped from the 1<sup>st</sup> cycle of 2.5 to  $1.4 \text{ mmol g}^{-1} \text{ h}^{-1}$  (3<sup>rd</sup> cycle) which is far worse than the initial measurement of  $5.9 \text{ mmol g}^{-1} \text{ h}^{-1}$  (Fig. 3a). The instability of Cu/TiO<sub>2</sub> (surface-load) for repeated usage is likely due to leaching and aggregation of the Cu NPs (Fig. S15†), thus reducing the efficiency of the photocatalytic activity.

The excellent and stable performance of Cu/TiO<sub>2</sub>-1.6 can be ascribed to the shorter pathway of the electron transfer from the TiO<sub>2</sub>/Cu interface to the Cu surface due to the embedment of Cu NPs in TiO<sub>2</sub>. As the Cu NPs are interdispersed within TiO<sub>2</sub>, clustering and leaching of the NPs are inhibited, keeping the

electron transportation pathway stable for prolonged usage of the photocatalyst. In view of elucidating the charge transportation mechanism, PL, EIS and PEC measurements were conducted. It is noted that PL arises from the recombination of free carriers<sup>42,43</sup> and its emission intensity reflects the efficiency of the charge transfer process. A drop in peak intensities was observed in both Cu/TiO<sub>2</sub> (surface-load) and Cu/TiO<sub>2</sub>-1.6, compared to TiO<sub>2</sub> as shown in Fig. 4a. This is due to the presence of Cu NPs which act as electron sinks to reduce electron-hole pair recombination. It was noted that Cu/TiO<sub>2</sub>-1.6 has a PL peak of slightly lower intensity as compared to Cu/TiO<sub>2</sub> (surface-load). The slightly more suppressed PL peak of Cu/TiO<sub>2</sub>-1.6 suggests reduced recombination of photo-generated electron-hole pairs. EIS was also used to evaluate the efficiency of the charge transfer process. A small radius suggests low charge transfer resistance,<sup>44,45</sup> usually an indication of large photocurrent due to the ease of more electrons traveling through the electrode and electrolyte. In the Nyquist diagram shown in Fig. 4b, the EIS measurements were collected for the three samples in the dark (without any light irradiation) and under UV light irradiation. It was revealed that under UV irradiation, smaller arcs were observed for all three samples, indicating

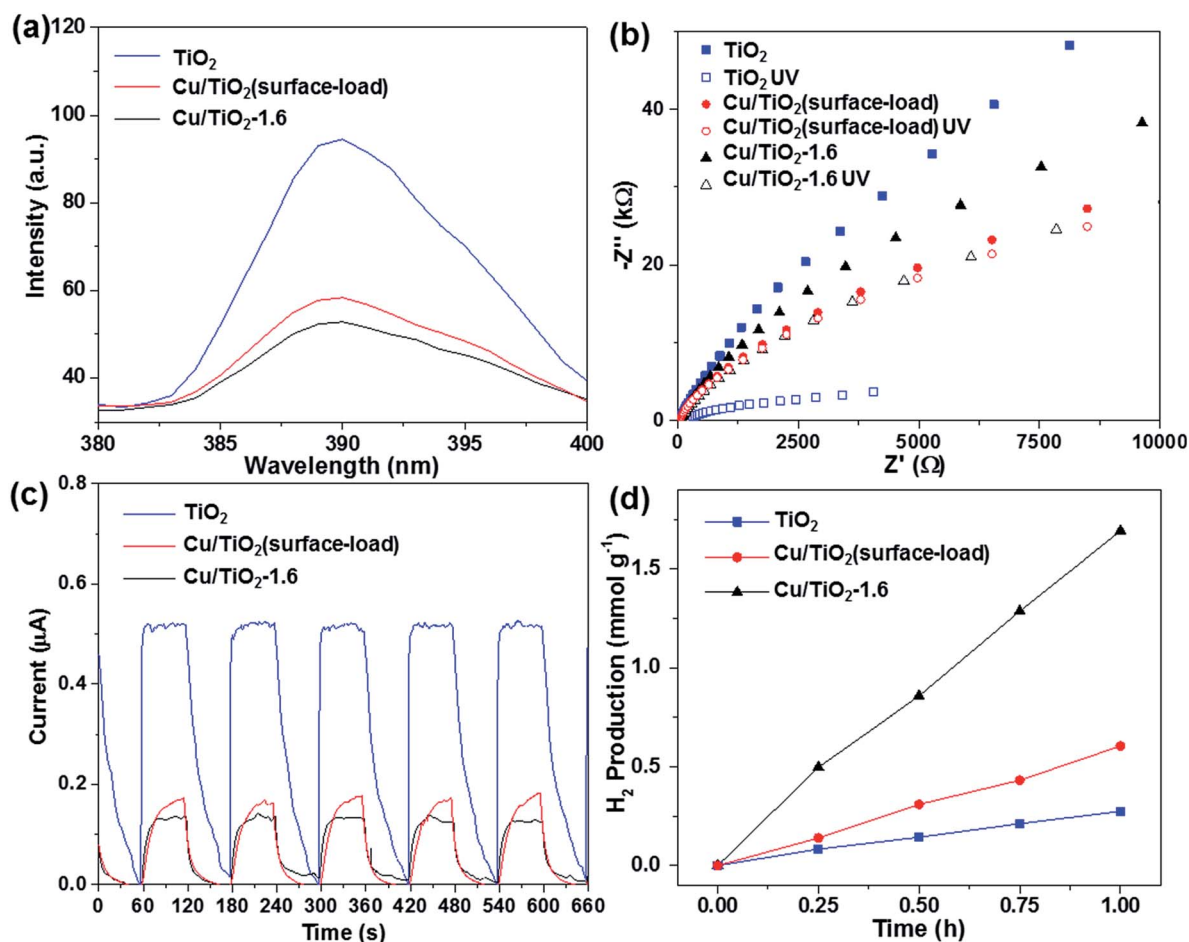


Fig. 4 (a) Photoluminescence spectra and (b) electrochemical impedance spectra of TiO<sub>2</sub>, Cu/TiO<sub>2</sub> (surface-load) and Cu/TiO<sub>2</sub>-1.6 in the dark and under UV irradiation. (c and d) Photocurrent response and concurrent H<sub>2</sub> production measurements of TiO<sub>2</sub>, Cu/TiO<sub>2</sub> (surface-load) and Cu/TiO<sub>2</sub>-1.6 under UV irradiation.

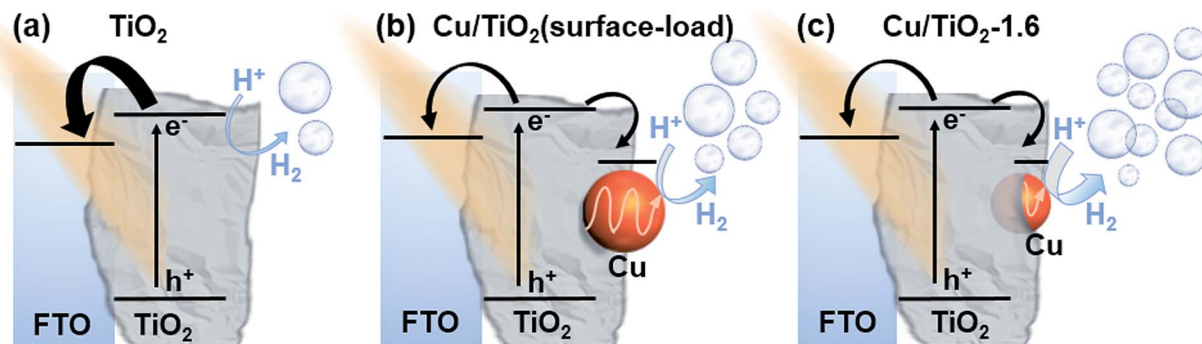


Fig. 5 Mechanism of charge transfer of  $\text{TiO}_2$ ,  $\text{Cu/TiO}_2$  (surface-load),  $\text{Cu/TiO}_2$ -1.6.

lower charge transfer resistance, which indicated higher PEC currents when illuminated with UV light (Fig. 4c). In addition,  $\text{Cu/TiO}_2$  (surface-load) and  $\text{Cu/TiO}_2$ -1.6 have higher charge transfer resistance as compared to  $\text{TiO}_2$ . It was noted that  $\text{TiO}_2$  exhibited the highest photocurrent of  $0.52 \mu\text{A}$  followed by  $\text{Cu/TiO}_2$  (surface-load) with  $0.17 \mu\text{A}$  and  $\text{Cu/TiO}_2$ -1.6 with  $0.13 \mu\text{A}$ . This is in agreement with the EIS result, where  $\text{TiO}_2$  with the lowest charge transfer resistance (Fig. 4b) exhibited the highest photocurrent (Fig. 4c).

These results, however, follow an inverse trend with respect to the PL measurements. Suppressed PL peaks are associated with an increase in the number of electrons available for the photocatalytic reaction due to reduced recombination.<sup>42</sup> The increase in the number of electrons is expected to result in an increase in photocurrent as more electrons are available to migrate to the electrode.<sup>46</sup> In this case,  $\text{Cu/TiO}_2$ -1.6 has the lowest PL peak intensity (Fig. 4a) but also a small photocurrent of  $0.13 \mu\text{A}$  (Fig. 4c). Since the photocurrent follows an inverse trend to the PL results, concurrent  $\text{H}_2$  production measurements and PEC were carried out to further investigate the electron movement. The  $\text{H}_2$  production measurements for all three samples were taken at every 15 min interval and plotted as shown in Fig. 4d. In an hour,  $\text{Cu/TiO}_2$ -1.6 demonstrated the highest  $\text{H}_2$  production amount of  $1.69 \text{ mmol g}^{-1}$ , followed by  $\text{Cu/TiO}_2$  (surface-load) and  $\text{TiO}_2$  with  $0.625$  and  $0.27 \text{ mmol g}^{-1}$ , respectively. The proposed mechanism for the electron charge transportation during the PEC and  $\text{H}_2$  measurements is illustrated as shown in Fig. 5. Comparing  $\text{TiO}_2$  and  $\text{Cu/TiO}_2$  (surface-load) samples, electron-hole pairs are being generated when irradiated with light. In the  $\text{TiO}_2$  sample (Fig. 5a), the electrons may either travel to the FTO or react with  $\text{H}^+$  ions to produce  $\text{H}_2$ . In the  $\text{Cu/TiO}_2$  (surface-load) sample (Fig. 5b), the electrons may travel to the FTO or to the Cu NPs and then react with  $\text{H}^+$  ions to produce  $\text{H}_2$ . Since the band position of Cu is below that of FTO ( $4.4 \text{ eV}$ )<sup>47,48</sup> due to a larger work function of Cu ( $4.7 \text{ eV}$ ), it is more feasible for the electrons to be transported to the Cu instead of FTO. In addition, the electrons in Cu NPs are unlikely to be transported back to FTO due to the lower band position of Cu. As such, the reduced photocurrent in  $\text{Cu/TiO}_2$  (surface-load) (Fig. 4c) is attributed to the presence of Cu NPs (electron sink) which prevents the electron movement from  $\text{TiO}_2$  to the FTO electrode. As more photo-generated electrons are transferred to the Cu NPs, the  $\text{H}_2$  production rate of  $\text{Cu/TiO}_2$  (surface-load)

increased as compared to  $\text{TiO}_2$  (Fig. 4d). Similarly for  $\text{Cu/TiO}_2$ -1.6, the Cu NPs draw electrons away from the FTO electrode, contributing to a low photocurrent (Fig. 4c). It is interesting to note that although  $\text{Cu/TiO}_2$ -1.6 and  $\text{Cu/TiO}_2$  (surface-load) demonstrated comparable PL and photocurrent, which suggests that both samples have a comparable number of electrons available for  $\text{H}_2$  production activity (Fig. 5b and c), the amount of  $\text{H}_2$  generated in  $\text{Cu/TiO}_2$ -1.6 is approximately 2.7 times higher (Fig. 4d). The enhanced  $\text{H}_2$  production rate in  $\text{Cu/TiO}_2$ -1.6 may be attributed to two factors: (i) the embedment of Cu NPs within the  $\text{TiO}_2$  and (ii) the small size of the Cu NPs. Due to the incorporation of small Cu NPs in  $\text{Cu/TiO}_2$ -1.6, the diffusion distance of charge carriers is significantly shortened. Hence, more electrons in  $\text{Cu/TiO}_2$ -1.6 would reach the surface compared to  $\text{Cu/TiO}_2$  (surface-load) in a given time, thereby enhancing the photocatalytic activity of  $\text{Cu/TiO}_2$ -1.6. The above results reveal that the enhanced  $\text{H}_2$  production rate in  $\text{Cu/TiO}_2$ -1.6 is attributed to the interdispersion and embedment of small Cu NPs which aid in the fast transportation of electrons from the  $\text{TiO}_2/\text{Cu}$  interface to the Cu surface.

## Conclusions

A straightforward approach using one-step hydrothermal to simultaneously realize *in situ* reduction and embedment of homogeneously interdispersed Cu within a  $\text{TiO}_2$  matrix for enhanced photocatalytic  $\text{H}_2$  production is demonstrated. The immobilization of the Cu NPs in the  $\text{TiO}_2$  matrix reduces the likelihood of clustering and leaching. Since the Cu NPs are embedded in  $\text{TiO}_2$ , intimate interfacial contact of  $\text{TiO}_2$  with Cu NPs results in the improvement of the charge carrier transportation from the  $\text{TiO}_2/\text{Cu}$  interface to the surface for photocatalytic reactions. An optimal peak size and concentration of  $4 \text{ nm}$  and a  $\text{Cu} : \text{TiO}_2$  ratio of  $1.6 : 1$  were found to exhibit the highest  $\text{H}_2$  production rate of approximately  $16 \text{ mmol g}^{-1} \text{ h}^{-1}$  with excellent stability for repeated and prolonged usage. It is also noteworthy that the enhanced photoredox and charge transport properties of the  $\text{Cu/TiO}_2$  hybrid compared to  $\text{Cu/TiO}_2$  synthesized by the conventional deposition-precipitation method are validated.

## Conflicts of interest

There are no conflicts of interest to declare.

## Acknowledgements

This work is supported by MOE R-263-000-C85-112 and R-263-000-D08-114 (Ministry of Education, Singapore).

## Notes and references

- 1 L. Yuan, C. Han, M.-Q. Yang and Y.-J. Xu, *Int. Rev. Phys. Chem.*, 2016, **35**, 1–36.
- 2 P. Zhang, T. Song, T. Wang and H. Zeng, *RSC Adv.*, 2017, **7**, 17873–17881.
- 3 S. Y. Tee, K. Y. Win, W. S. Teo, L.-D. Koh, S. Liu, C. P. Teng and M.-Y. Han, *Adv. Sci.*, 2017, **4**, 1600337.
- 4 M.-Q. Yang, C. Han and Y.-J. Xu, *J. Phys. Chem. C*, 2015, **119**, 27234–27246.
- 5 N. Zhang, M.-Q. Yang, S. Liu, Y. Sun and Y.-J. Xu, *Chem. Rev.*, 2015, **115**, 10307–10377.
- 6 L. Guo, Z. Yang, K. Marcus, Z. Li, B. Luo, L. Zhou, X. Wang, Y. Du and Y. Yang, *Energy Environ. Sci.*, 2018, **11**, 106–114.
- 7 H. He, J. Lin, W. Fu, X. Wang, H. Wang, Q. Zeng, Q. Gu, Y. Li, C. Yan, B. K. Tay, C. Xue, X. Hu, S. T. Pantelides, W. Zhou and Z. Liu, *Adv. Energy Mater.*, 2016, **6**, 1600464.
- 8 H. G. Yang, C. H. Sun, S. Z. Qiao, J. Zou, G. Liu, S. C. Smith, H. M. Cheng and G. Q. Lu, *Nature*, 2008, **453**, 638.
- 9 H. Xu, S. Ouyang, L. Liu, P. Reunchan, N. Umezawa and J. Ye, *J. Mater. Chem. A*, 2014, **2**, 12642–12661.
- 10 T. J. Wong, F. J. Lim, M. Gao, G. H. Lee and G. W. Ho, *Catal. Sci. Technol.*, 2013, **3**, 1086–1093.
- 11 L. Zhu, C. F. Tan, M. Gao and G. W. Ho, *Adv. Mater.*, 2015, **27**, 7713–7719.
- 12 C. Liu, J. Tang, H. M. Chen, B. Liu and P. Yang, *Nano Lett.*, 2013, **13**, 2989–2992.
- 13 S. G. Kumar and L. G. Devi, *J. Phys. Chem. A*, 2011, **115**, 13211–13241.
- 14 Y. Dou, J. Zhou, A. Zhou, J.-R. Li and Z. Nie, *J. Mater. Chem. A*, 2017, **5**, 19491–19498.
- 15 D. Ding, K. Liu, S. He, C. Gao and Y. Yin, *Nano Lett.*, 2014, **14**, 6731–6736.
- 16 B. Pan, S. Luo, W. Su and X. Wang, *Appl. Catal., B*, 2015, **168–169**, 458–464.
- 17 X. Yan, C. Xue, B. Yang and G. Yang, *Appl. Surf. Sci.*, 2017, **394**, 248–257.
- 18 M. Zhu, X. Cai, M. Fujitsuka, J. Zhang and T. Majima, *Angew. Chem., Int. Ed.*, 2017, **56**, 2064–2068.
- 19 M. Gao, P. K. N. Connor and G. W. Ho, *Energy Environ. Sci.*, 2016, **9**, 3151–3160.
- 20 T. Zhu, W. Li Ong, L. Zhu and G. Wei Ho, *Sci. Rep.*, 2015, **5**, 10601.
- 21 K. Liu, Z. Zhang, N. Lu and B. Dong, *ACS Sustainable Chem. Eng.*, 2017, **6**, 1934–1940.
- 22 R. Li, S. Wu, X. Wan, H. Xu and Y. Xiong, *Inorg. Chem. Front.*, 2016, **3**, 104–110.
- 23 H. Tong, S. Ouyang, Y. Bi, N. Umezawa, M. Oshikiri and J. Ye, *Adv. Mater.*, 2012, **24**, 229–251.
- 24 J. Low, J. Yu, M. Jaroniec, S. Wageh and A. A. Al-Ghamdi, *Adv. Mater.*, 2017, **29**, 1601694.
- 25 F. Wang, Q. Li and D. Xu, *Adv. Energy Mater.*, 2017, **7**, 1700529.
- 26 X. He and W.-N. Wang, *J. Mater. Chem. A*, 2018, **6**, 932–940.
- 27 F. Wang, R. J. Wong, J. H. Ho, Y. Jiang and R. Amal, *ACS Appl. Mater. Interfaces*, 2017, **9**, 30575–30582.
- 28 Y. Liu, Q. Yao, X. Wu, T. Chen, Y. Ma, C. N. Ong and J. Xie, *Nanoscale*, 2016, **8**, 10145–10151.
- 29 H. Li, Z. Bian, J. Zhu, Y. Huo, H. Li and Y. Lu, *J. Am. Chem. Soc.*, 2007, **129**, 4538–4539.
- 30 S. Shuang, R. Lv, Z. Xie and Z. Zhang, *Sci. Rep.*, 2016, **6**, 26670.
- 31 H. Zhu, N. Goswami, Q. Yao, T. Chen, Y. Liu, Q. Xu, D. Chen, J. Lu and J. Xie, *J. Mater. Chem. A*, 2018, **6**, 1102–1108.
- 32 M. Gao, S. W. L. Ng, L. Chen, M. Hong and G. W. Ho, *J. Mater. Chem. A*, 2017, **5**, 10909–10916.
- 33 S. Jo, P. Verma, Y. Kuwahara, K. Mori, W. Choi and H. Yamashita, *J. Mater. Chem. A*, 2017, **5**, 21883–21892.
- 34 H. Shi, S. Zhang, X. Zhu, Y. Liu, T. Wang, T. Jiang, G. Zhang and H. Duan, *ACS Appl. Mater. Interfaces*, 2017, **9**, 36907–36916.
- 35 W. J. Foo, C. Zhang and G. W. Ho, *Nanoscale*, 2013, **5**, 759–764.
- 36 S. Xiao, P. Liu, W. Zhu, G. Li, D. Zhang and H. Li, *Nano Lett.*, 2015, **15**, 4853–4858.
- 37 A. Kubacka, M. Fernández-García and G. Colón, *Chem. Rev.*, 2012, **112**, 1555–1614.
- 38 G. Grass, C. Rensing and M. Solioz, *Appl. Environ. Microbiol.*, 2011, **77**, 1541–1547.
- 39 L. Argueta-Figueroa, R. A. Morales-Luckie, R. J. Scougall-Vilchis and O. F. Olea-Mejía, *Prog. Nat. Sci.: Mater. Int.*, 2014, **24**, 321–328.
- 40 C. K. N. Peh, M. Gao and G. W. Ho, *J. Mater. Chem. A*, 2015, **3**, 19360–19367.
- 41 W. Wang, S. Liu, L. Nie, B. Cheng and J. Yu, *Phys. Chem. Chem. Phys.*, 2013, **15**, 12033–12039.
- 42 Y. Dou, S. Zhang, T. Pan, S. Xu, A. Zhou, M. Pu, H. Yan, J. Han, M. Wei, D. G. Evans and X. Duan, *Adv. Funct. Mater.*, 2015, **25**, 2243–2249.
- 43 J. Tian, Y. Sang, Z. Zhao, W. Zhou, D. Wang, X. Kang, H. Liu, J. Wang, S. Chen, H. Cai and H. Huang, *Small*, 2013, **9**, 3864–3872.
- 44 M. Wang, D. Zheng, M. Ye, C. Zhang, B. Xu, C. Lin, L. Sun and Z. Lin, *Small*, 2015, **11**, 1436–1442.
- 45 F.-X. Xiao, S.-F. Hung, J. Miao, H.-Y. Wang, H. Yang and B. Liu, *Small*, 2015, **11**, 554–567.
- 46 J. Zhang and F.-X. Xiao, *J. Mater. Chem. A*, 2017, **5**, 23681–23693.
- 47 A. M. Ganose, K. T. Butler, A. Walsh and D. O. Scanlon, *J. Mater. Chem. A*, 2016, **4**, 2060–2068.
- 48 H.-Q. Luo, X.-H. Xing, P. Zhang, Z.-S. Yan, Q.-F. Zhou, Y. Gong and J.-H. Lin, *Dalton Trans.*, 2017, **46**, 7866–7877.